Pattern formation during diffusional transformations in the presence of triple junctions and elastic effects

2009 J. Phys.: Condens. Matter 21 464106

(http://iopscience.iop.org/0953-8984/21/46/464106)

IOP Publishing Journal of Physics: Condensed Matter

J. Phys.: Condens. Matter **21** (2009) 464106 (10pp) doi:10.1088/0953-8984/21/46/464106

Pattern formation during diffusional transformations in the presence of triple junctions and elastic effects

E A Brener[1], G Boussinot[1], C Hüter[1], M Fleck[1], D Pilipenko[1], R Spatschek[2] and D E Temkin[1]

[1] Institut für Festkörperphysik Forschungszentrum Jülich, Jülich, Germany
[2] Interdisciplinary Center for Advanced Materials Simulations, Ruhr-Universität Bochum, Germany

E-mail: d.pilipenko@fz-juelich.de

Received 27 April 2009, in final form 20 July 2009
Published 27 October 2009
Online at stacks.iop.org/JPhysCM/21/464106

Abstract

We compare different scenarios for dendritic melting of alloys with respect to the front propagation velocity. In contrast to conventional dendritic growth, selection can here be also due to the presence of a grain boundary or coherence strains, and the propagation speed is higher. The most favorable situation is partial melting, where two parabolic fronts, one melting and one solidifying interface, are moving together, since the process is then determined by diffusion in the thin liquid layer. There, and also in phase field simulations of melting in peritectic and eutectic systems, we observe a rotation of the triple junction relative to the growth direction. Finally, we discuss the role of elastic effects due to density and structural differences on solid-state phase transformations, and we find that they significantly alter the selection principles. In particular, we obtain free dendritic growth even with isotropic surface tension. This is investigated by Green's function methods and a phase field approach for growth in a channel and illustrated for the formation of a twin phase.

1. Introduction

The kinetics of diffusion-limited phase transitions is of central interest in the vast field of materials science, which can lead to surprising dynamical behavior. In particular, solidification processes have been studied extensively during the past decades both from an experimental and a theoretical point of view, which has led to a thorough understanding of many aspects of these also technologically important transformations.

Based on the initial observation that a slightly undercooled liquid cannot solidify with constant velocity as a planar front, since the released latent heat or rejected impurities from the propagating solid cannot be efficiently transported away by diffusion, Ivantsov made the surprising discovery that a parabolic front in principle forms a steady-state solution of the problem [1]. This prediction was in agreement with experimental observations where a constant transformation rate can be found, and polished micrograph sections showed 'dendritic' patterns with tips similar to the Ivantsov parabola. However, in this first solution the effect of surface tension was neglected, and a generalization was far from being straightforward. Also, the theory predicted only a one-parameter family of solutions, which determines only the Peclet number, essentially the product of the dendrite tip radius and its growth speed, as a function of the undercooling, but does not fix each of these observables separately; this is in contrast to experimental findings, which suggested a well-selected propagation speed and scale of the patterns. It took a long time to finally understand that surface tension, and in particular its anisotropy, plays a central role in dendritic growth, see for example [2, 3]. In particular, it was found that with purely isotropic surface tension dendritic solutions do not even exist, and instead so-called doublon structures emerge [4, 5]. Since then, the concept of dendritic growth and the notion of surface tension anisotropy are intimately tied together.

Conceptually, many other processes in materials science can be controlled by bulk diffusion, and it is therefore not surprising that similar concepts for theoretical modeling can

be applied. One example is the melting of an overheated solid, where also the propagation of parabolic melt fronts is possible; this has also been observed experimentally, see, e.g., [6] and references therein. A typical difference between solidification and melting is, however, that it is usually much easier to undercool a liquid than to overheat a solid. Similarly, even for solid-state transformations where dendrite-like patterns can grow, such as, for example, in Widmanstaetten structures, the analogy with solidification has been known for a long time; it has recently been reviewed in [7]. It is therefore natural to believe that also in these processes aspects of microscopic solvability theory, and in particular surface tension anisotropy, should play an important role.

It is a major goal of the present paper to demonstrate that, in particular, during the latter processes very different selection mechanisms than surface tension anisotropy can become dominant, which sheds new light on selection principles in diffusion-limited growth. We therefore discuss here several different processes to emphasize the variety of selection mechanisms and to compare them to each other.

For melting processes the presence of heterogeneities in the mother solid phase can lead to dramatic changes of the morphology. Starting from the nucleation regime, it is usually favorable for a new phase to appear at an interface or a grain boundary, since this is energetically the most favorable location and thus the nucleation barrier is minimized. The emergence of triple junctions is therefore a natural consequence, and it can lead to substantial changes of the growth kinetics as well. In particular, it has been shown recently [8] that the presence of a triple junction at the tip of the melting zone leads to an entirely different selection mechanism, since the triple junction produces a very strong perturbation of the liquid–solid interfaces, and weak anisotropy effects can be neglected. One feature is that, on the small scales that appear here, mass transport can also take place efficiently along grain boundaries, especially since diffusion within the adjacent solid phases is usually slow. Another aspect is that, especially for melting between two grains of the same material, elastic effects can become important, since the short diffusion length in the solid can lead to strong concentration gradients in propagating solid–liquid interfaces due to the impurity pile-up in the solid phases.

In the case of solid–solid transformations the new ingredient in the selection theory is the elastic field [9]. In this case, dendritic patterns are also selected even without anisotropy of the surface energy required by classical dendritic growth theory. Although the elastic effects also introduce an 'effective anisotropy', the physics and structure of selection theory for the two mechanisms, anisotropy of surface energy and elastic effects, are fundamentally different. Moreover, elastic effects lead to a much more robust selection mechanism compared to tiny effects of anisotropy of surface energy.

To shed light on these different selection mechanisms in a comparative manner, this paper is organized as follows: section 2 reviews recent findings concerning the propagation of melt fronts in dilute binary alloys, emphasizing the role of grain boundaries and coherence stresses, which can serve as an effective driving force. Here, the focus is on analytical scaling relations to understand the efficiency of the different scenarios. One element, a rotation of the triple junction due to grain boundary diffusion that appears as a symmetry-breaking process, is similarly observed in peritectic and eutectic systems, see section 3. In contrast to the preceding section, where even in the presence of a grain boundary the two adjacent grains are assumed to belong to the same solid phase, the melt phase appears here between two different phases with unequal equilibrium concentrations. Here, we will highlight results from phase field simulations. Finally, structural transformations and density differences are another important source for elastic stresses during solid-state transformations, and to date their influence on the growth kinetics in dendrite-like solid-state transformations is largely unexplored from a theoretical point of view; they will be investigated in section 4.

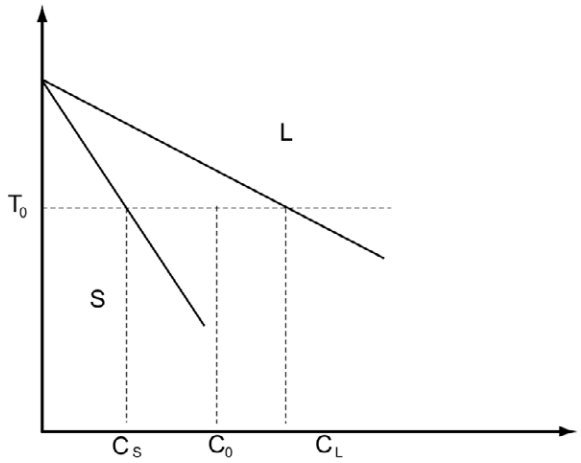

Figure 1. Schematic representation of the phase diagram. The solid is quenched into the two-phase region and starts to melt.

The overall aim of the present paper is to summarize our recent results on heterogeneous systems and to put them into a more global context, with a particular focus on new selection mechanisms in dendrite-like growth.

2. Dendritic melting of alloys

The theory of dendritic growth led to an enormous success in the understanding of solidification patterns in many pure materials and alloys; this triggered many theoretical, numerical and experimental investigations. From a fundamental point of view, the reverse process of diffusion-limited *melting* could follow similar principles, but it immediately turns out that this process is not very favorable, at least in the case of alloys: the propagation of a dendrite-like melt front would require the diffusive transport of impurities in the surrounding solid phase and therefore this process is significantly slower than dendritic solidification. We could imagine an initially solid binary system that is quenched into the miscibility gap, where the phase separation process starts (see figure 1). The theory of dendritic growth then predicts a scaling of the steady-state velocity of the propagating parabolic front (see figure 2(a)) according to [10]

$$V \sim \frac{D_s^2 \Delta^4}{D d_0} \alpha^{7/4}, \tag{1}$$

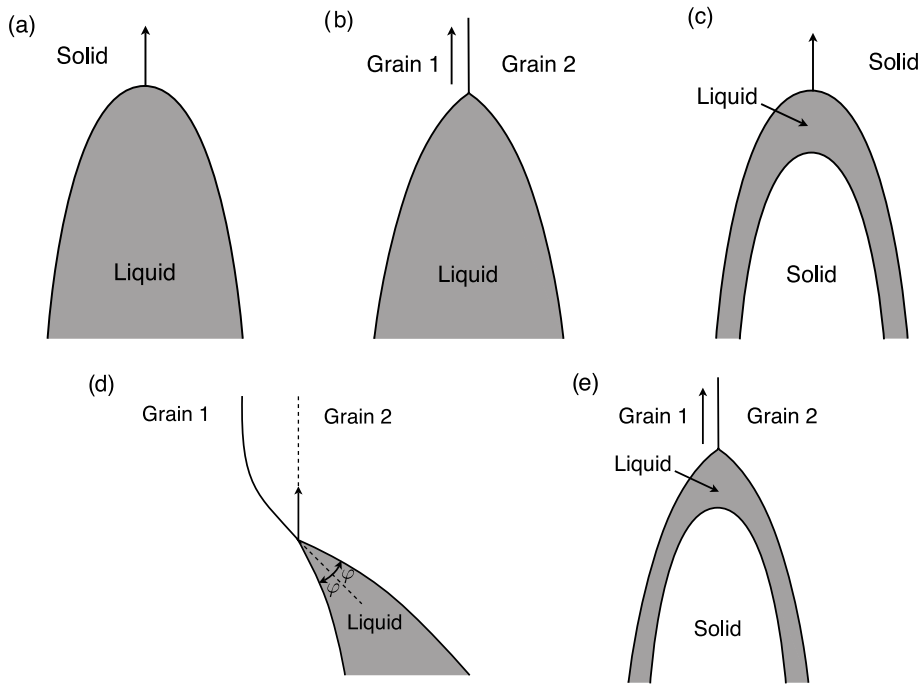

Figure 2. Schematic representation of the different melting processes: (a) dendritic melting with only one front. (b) Dendritic melting along a grain boundary. (c) Liquid film migration leads to the appearance of two confocal parabolic fronts. The first one is a melting, the second a solidification front. (d) Partial melting along a grain boundary. (e) Liquid film migration along a grain boundary.

where $\Delta = (c_0 - c_S)/(c_L - c_S)$ is the dimensionless driving force with c_L and c_S being the liquidus and solidus concentrations as depicted in the equilibrium phase diagram figure 1. The diffusion coefficient in the solid D_s is much smaller than the corresponding value in the melt and $D_s \ll D$; d_0 denotes the chemical capillarity length. Notice that the growth velocity is selected by the anisotropy of surface tension, which is expressed here through the small parameter α. We note that the process would be significantly faster in pure materials, where the phase transition is induced by an overheating of the solid, since heat diffusion in solid and liquid (neglecting convection) is basically equally fast.

It is an important observation that for melting along a grain boundary (see figure 2(b)) the selection is controlled by the finite dihedral angles at the triple junction, which is a much stronger selection mechanism than anisotropy effects [8]. In particular, dendritic melting is even possible for purely isotropic surface tension, where otherwise only doublon patterns would appear. The propagation velocity

$$V \sim \frac{D_s^2 \Delta^4}{D d_0} \tag{2}$$

is therefore significantly higher, as the anisotropy factor α does not appear, but nevertheless the process is still controlled by the slow diffusion in the solid phase.

There is, however, another possible kinetic path towards equilibrium that is controlled only by diffusion in the liquid phase, which is related to the phenomenon of *liquid film migration* (LFM). The early observations of liquid film migration have been made during sintering in the presence of a liquid phase [11] or during partial melting of alloys [12, 13]. In LFM, one crystal is melting and another one is solidifying. Both solid–liquid interfaces move together with the same velocity [14], as depicted in figure 2(c). Typically, the characteristic velocity of atomic kinetics at the interfaces is much larger than the migration velocity; hence both solids should be locally in thermodynamic equilibrium with the liquid phase at the interfaces. On the other hand, these local equilibrium states should be different for the two interfaces to provide the driving force for the process. It is well accepted [13, 15] that the difference of the equilibrium states at the melting and solidification fronts is due to the coherence strain energy, which is important only at the melting front because of the sharp concentration profile ahead of the moving melting front. The solute atoms diffuse ahead of the moving film and the coherence strain energy in such a frontal diffusion zone arises from the solute misfit. Consequently, the equilibrium liquid composition at the melting front, which depends on the coherence strain energy and on the curvature of the front, differs from the liquid composition at the unstressed and curved solidification front. This leads to the necessary gradient of the concentration across the liquid film and the process is controlled by the diffusion in the film.

Thus, a theoretical description of LFM requires the solution of a free boundary problem for two combined moving solid–liquid interfaces with a liquid film in between. This was done in [16] and it was found that two confocal parabolic fronts can move together with the same velocity. There, however, capillary, kinetic and crystallographic effects at the interfaces were neglected. Similarly to conventional dendritic growth, only the Peclet numbers of the two parabolas were found within this approximation, but the steady-state velocity

remained undetermined at that stage. Following concepts of solvability theory (see, for example, [2, 3, 17]), capillarity is a singular perturbation and the anisotropy of the surface energy is a prerequisite for the existence of the solution in this theory. In [14] we extended the selection theory for the process of liquid film migration where the strong diffusion interaction between melting and solidification fronts plays a crucial role. We found that the propagation velocity scales as

$$V \sim \frac{Db^2\Delta^3}{d_0}\alpha^{5/4}, \qquad \Delta \ll \alpha^{1/2}, \tag{3}$$

$$V \sim \frac{Db^2\Delta^2}{d_0}\alpha^{7/4}, \qquad \Delta \gg \alpha^{1/2}, \tag{4}$$

where b is the dimensionless constant which describes the coherence strain energy [15].

The presence of a grain boundary can again have a substantial influence on the melting kinetics. Energetically, the grain boundary is the most favorable location for nucleation of the melt, which can subsequently grow as depicted in figure 2(d) with spontaneously broken symmetry; this situation is analyzed in detail in [18]. Again, the presence of the triple junction in this geometry drastically changes the structure of the theory and leads to a very strong perturbation of the solid–liquid interface; the anisotropy of surface tension does not play an important role in such processes [8, 19]. We emphasize that the triple junction is rotated together with the entire structure. This is possible due to diffusion along the grain boundary, which therefore deforms. The problem was solved in the lubrication approximation which allows us to reduce the originally nonlocal problem to a local and analytically tractable problem. For small driving forces Δ and for not too small angles, $\Delta/\varphi \ll 1$, the steady-state velocity of this process scales as [18]

$$V \sim \frac{Db^2\Delta^3}{d_0}, \tag{5}$$

thus, one can use the scaling given by equation (3), formally setting $\alpha \sim 1$ [8]. We note that the velocities of different processes increase from equations (1) to (5). From the preceding results we can speculate that the velocity of the LFM growth mode with a triple junction, as sketched in figure 2(e), should also scale according to equation (5), but a detailed investigation is beyond the scope of the present paper.

3. Melting along inter-phase boundaries in peritectic and eutectic systems

As a more complicated example that still shows similar elements as in the cases mentioned above, we investigate here the melting along a solid–solid interface in a peritectic and a eutectic system as depicted in figure 3. Instead of a boundary between grains of the same phase, the melting is here initiated between the two solid phases γ and δ slightly above the peritectic or eutectic temperature. This melting has been studied theoretically in both cases in [20].

In peritectic melting and eutectic melting along the solid–solid interface, the driving force is provided by the difference between the equilibrium concentration of the liquid (L) $c_{L\gamma}$ at the γ/L interface and $c_{L\delta}$ at the δ/L interface. In the growing liquid phase, fast diffusion provides an efficient mechanism for the process to take place. At the triple junction, the steady-state solution for the diffusion field in the liquid requires a rotation of the whole structure, and the solid–solid interface then adopts an angle with respect to the growth direction. This angle can be calculated within a lubrication approximation and its value depends only on the concentration jumps (see figure 4 for schematic phase diagrams of peritectic and eutectic alloys) at the solid–liquid interfaces, $\Delta c_\gamma = c_{\mathrm{P(E)}} - c_\gamma$ and $\Delta c_\delta = c_{\mathrm{P(E)}} - c_\delta$, and on the contact angles at the triple junction. Moreover, this rotation of the solid–solid interface at the triple junction is used as a boundary condition for the problem of diffusion along the γ/δ interface, which allows us to calculate a profile that is asymptotically aligned with the propagation direction. Far behind the triple junction, the solid–liquid interfaces are parabolic.

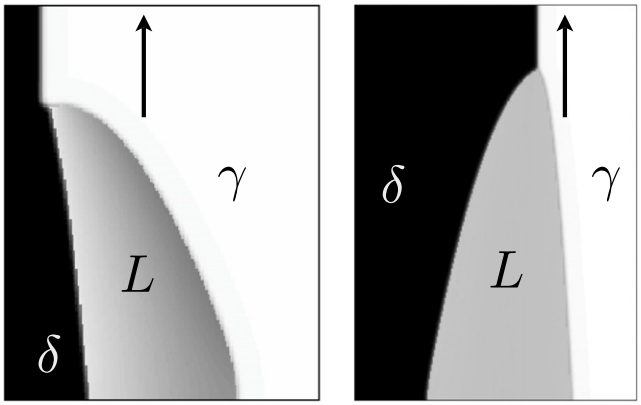

Figure 3. Left: melting of a peritectic alloy along the solid–solid interface (γ/δ interface). The solid peritectic phase γ (white) melts and the solid primary phase δ (black) solidifies (the liquid phase L is shown in gray). The arrow indicates the direction of propagation. Right: melting of a eutectic alloy along the solid–solid interface. In this case, both solid phases γ and δ melt.

According to the peritectic phase diagram, the concentration jumps at the solid–liquid interfaces Δc_γ and Δc_δ are of the same sign. The consequence is that, behind the triple junction, the γ phase melts and the δ phase solidifies, leading to the migration of the liquid film. This process is close to the partial melting along a grain boundary (figure 2(d)) where the driving force is due to elastic interactions in the melting grain. In the eutectic system, the situation is different: the concentration jumps at the solid–liquid interfaces are of opposite sign and both solid phases γ and δ melt. In this sense, this process is close to the dendritic melting along a grain boundary (figure 2(b)), but it is controlled by the diffusion in the liquid.

In figure 3 typical patterns obtained from phase field simulations of the melting of peritectic alloys (left) and eutectic alloys (right) along the γ/δ interface are presented. Phase field methods have been widely applied to peritectic and eutectic systems. Indeed, this is an efficient tool to model solidification microstructures (for a review see, for example, [21]). For peritectic and eutectic systems, the phase field method has proven its efficiency to reproduce complex

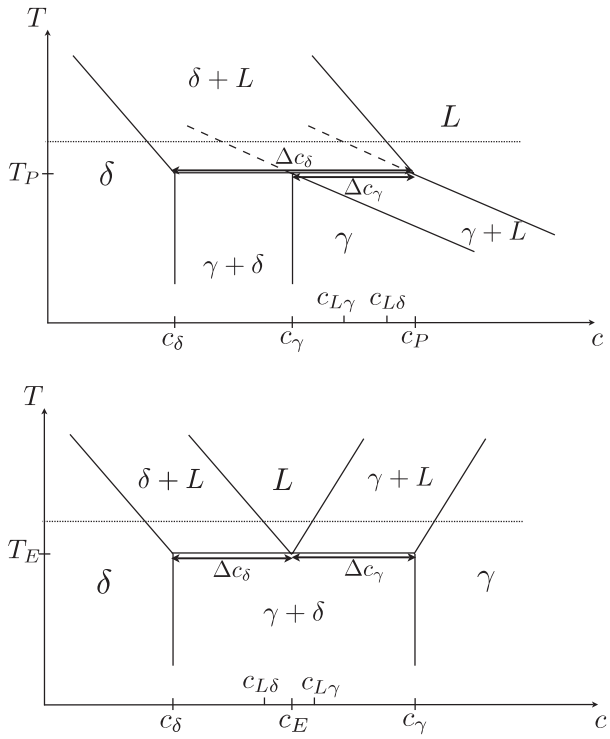

Figure 4. Top: schematic peritectic phase diagram. The dashed lines are the metastable extension of the $(\gamma + L)$ two-phase region. The dotted line corresponds to the operating temperature above the peritectic temperature T_{P}. Bottom: schematic eutectic phase diagram. The light line corresponds to the operating temperature above the eutectic temperature T_{E}.

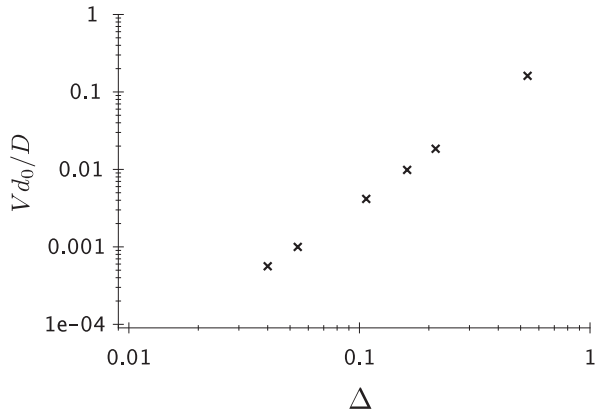

Figure 5. Dimensionless steady-state velocity Vd_0/D versus dimensionless driving force Δ. On this logarithmic plot, the slope is close to 2, which is the analytically predicted value.

solidification microstructures [22, 23]. Here, three phase fields are defined [24, 25]: p_γ, p_δ and p_L ($p_i = 1$ in the phase i and 0 otherwise); their sum is equal to 1. The underlying model used here was developed by Folch and Plapp [26] to study the directional solidification of eutectic alloys. The phase fields, which are non-conserved order parameters, obey a relaxation equation and the concentration obeys a diffusion equation (we refer to equations (4.1) and (4.2) in [26] for explicit formulae). The diffusion coefficient is proportional to the liquid phase field p_L and no diffusion is thus present in the solid phases. For simplicity, the surface tensions are equal for all interfaces, and they divide the triple junction into three sectors with equal angles.

The presented patterns in figure 3 are close to the schematic pictures discussed in [20]. In particular, one can observe the rotation of the γ/δ interface in the vicinity of the triple junction in the peritectic system (left panel of figure 3). We note that the phase field model literally only includes bulk diffusion in the liquid phase, but in the region of the triple junction there is a remaining effective surface diffusion taking place on the scale of the phase field interface thickness, since the diffusion coefficient varies smoothly there. This allows the γ/δ interface to adopt an angle with respect to the growth direction, on a scale that is directly related to the interface thickness; this is qualitatively similar to [20], where it is shown that the scale on which the γ/δ is reoriented depends on the solid–solid interface diffusivity.

In the eutectic system (right panel of figure 3), the rotation of the triple junction is less pronounced. However, the pattern is clearly asymmetric. This is due to the phase diagram used in this simulation. When $\Delta c_\gamma/\Delta c_\delta = -1$ and for equal surface tensions, the γ/δ interface is a symmetry axis of the melting process and becomes straight (in contrast, the rotation is always present in the peritectic system). In figure 3, we have $\Delta c_\gamma/\Delta c_\delta = -3$, and therefore the pattern is asymmetric. However, the asymmetry of the phase diagram is too weak for the reorientation of the γ/δ interface to be visible.

Finally, we have investigated the dependence of the steady-state velocity on the dimensionless driving force $\Delta = (c_{L\gamma} - c_{L\delta})/(c_\gamma - c_\delta)$ for the eutectic melting along the solid–solid interface. The concentrations used for the normalization of the driving force c_γ and c_δ are the solid concentrations at the eutectic temperature. The driving force Δ is the magnitude of the deviation from eutectic equilibrium where $c_{L\gamma} = c_{L\delta} = c_{\mathrm{E}}$. Here, a linear dependence of the equilibrium concentrations on temperature is assumed. Furthermore, the concentration jumps Δc_γ and Δc_δ are taken independent of the temperature (parallel liquidus and solidus lines) with $\Delta c_\gamma/\Delta c_\delta = -1$. Finally, the liquidus and solidus slopes are assumed to be opposite for γ and δ, which makes the phase diagram completely symmetric with respect to c_{E}. In figure 5, the dimensionless steady-state velocity Vd_0/D is plotted versus the dimensionless driving force Δ on a logarithmic scale, with V being the velocity, d_0 is the average of capillary lengths for liquid–solid interfaces and D is the diffusion coefficient in the liquid phase. The observed slope is close to 2, which is the analytically expected value from [20]. Thus we have a good agreement between phase field simulations and analytical results obtained within a lubrication approximation.

4. Solid–solid transformations

There are many parallels between solid-state transformations and solidification or melting processes; in particular, the limiting case for purely diffusion-limited growth is equally applicable to both types of transitions [7]. Under many

circumstances, however, elastic effects can become crucial in solid-state transformations and their relevance for the growth kinetics will be discussed in this section.

Historically, solvability theory has been very successful in predicting certain properties of dendritic growth and a number of related phenomena (see, for example, [2, 3, 17, 27]), and the purpose is here to shed light on the influence of structural changes and density differences, which provoke elastic stresses, on dendritic growth in solids controlled by heat diffusion.

First, we will employ Green's function methods to eliminate *both* the thermal and elastic fields, which significantly simplifies the problem, and we obtain, as in the classical dendritic growth theory, a single integro-differential equation for the steady-state shape of the interface which takes into account elastic effects. Later, we also present results from phase field simulations. We investigate here only isotropic elasticity and surface tension in the framework of symmetrical models; this is not only a simplification of the problem (in particular since faceting can be pronounced in solid–solid transformations [7]) but also emphasizes that the selection behavior is significantly altered in comparison to classical dendritic growth, because we obtain steady-state (dendritic) solutions even without the anisotropy of surface tension, which is a major result of the present investigations. Also, we restrict our analysis here to pure materials; many results can directly be interpreted also in the framework of alloys, but we focus here on diffusion-limited growth with equal (thermal) diffusivity in all solid phases; for the sake of clarity we will therefore use the nomenclature of heat instead of impurity diffusion.

4.1. Thermodynamics of the model

Let us consider the growth of a new β phase (low temperature phase) inside a mother α phase. We denote the characteristic lattice strain (also known as the stress-free strain tensor), associated with the phase transition, by ϵ^0_{ik}. The free energy density in the initial α-phase is

$$F_\alpha = F^0_\alpha(T) + \frac{E}{2(1+\nu)}\left(\frac{\nu}{1-2\nu}\epsilon^2_{ii} + \epsilon^2_{ik}\right), \tag{6}$$

where $F^0_\alpha(T)$ is the free energy density without elastic effects, which depends only on the temperature T, ϵ_{ik} are the components of the strain tensor, and E and ν are the elastic modulus and Poisson ratio, respectively. The free energy density of the growing β phase is given by

$$F_\beta = F^0_\beta(T) + \frac{E}{2(1+\nu)} \times \left(\frac{\nu}{1-2\nu}(\epsilon_{ii}-\epsilon^0_{ii})^2 + (\epsilon_{ik}-\epsilon^0_{ik})^2\right). \tag{7}$$

Here, we neglect the difference between the elastic coefficients in the two phases. We also assume that the elastic effects are small, i.e. $\epsilon^0_{ik} \ll 1$. Since in our description the reference state for both phases is the undeformed initial phase, the coherence condition at the interface is $u^{(\alpha)}_i = u^{(\beta)}_i$, where u_i is the displacement vector. Mechanical equilibrium at the interface demands $\sigma^{(\alpha)}_{nn} = \sigma^{(\beta)}_{nn}$ and $\sigma^{(\alpha)}_{n\tau} = \sigma^{(\beta)}_{n\tau}$, $\sigma^{(\alpha)}_{ns} = \sigma^{(\beta)}_{ns}$. Here, the indices n and τ, s denote the normal and two tangential directions with respect to the interface. In the general case of curved interfaces, the surface energy γ has also to be incorporated, and the phase equilibrium condition for each interface point in the case of isotropic surface energy is

$$\tilde{F}_\alpha - \tilde{F}_\beta - \gamma\kappa = 0, \tag{8}$$

where κ is the local curvature of the interface. The coherence constraint implies the appearance of a new potential, $\tilde{F} = F - \sigma_{nn}\epsilon_{nn} - 2\sigma_{n\tau}\epsilon_{n\tau} - 2\sigma_{ns}\epsilon_{ns}$, which is conceptually related to the Legendre transformation between the free energy and the Gibbs free energy in classical thermodynamics [28]. Notice that elastic stresses arise here only due to internal interfaces between α and β, and the strain field can be written as an integral along the interface in the spirit of Green's function method.

4.2. Diffusion-limited growth

We introduce the dimensionless temperature field $w = C(T - T_\infty)/L$, where L is the latent heat, C is heat capacity and T_∞ is the temperature in the α phase far away from the interface. The temperature field w obeys the following heat diffusion equation and boundary conditions at the α/β interface:

$$D_t\nabla^2 w = \partial w/\partial t, \tag{9}$$

$$V_n = D_t\mathbf{n}\cdot(\nabla w_\beta|_{\rm int} - \nabla w_\alpha|_{\rm int}), \tag{10}$$

$$w|_{\rm int} = \Delta - d_0\kappa + T_{\rm eq}C\delta\tilde{F}_{\rm el}/L^2, \tag{11}$$

where $d_0 = \gamma T_{\rm eq}C/L^2$ is the capillarity length, D_t is the thermal diffusion constant and $T_{\rm eq}$ is the equilibrium temperature for the flat interface without elastic effects, i.e. it is determined by the condition $F^0_\alpha(T_{\rm eq}) = F^0_\beta(T_{\rm eq})$. We also introduce the dimensionless undercooling $\Delta = C(T_{\rm eq} - T_\infty)/L$ and the elastic energy difference $\delta\tilde{F}_{\rm el} = \tilde{F}_\alpha - \tilde{F}_\beta - F^0_\alpha + F^0_\beta$. The thermal field can be eliminated by using Green's function techniques (see, for example, [29]), and consequently together with a proper Green's tensor $G_{ik}(\mathbf{r}, \mathbf{r}')$ for the elastic field, one can write a single integro-differential equation for the shape of the solid–solid interface. For details, we refer to [9].

4.3. Shear transitions in free growth

Let us now consider the simple type of transition in hexagonal crystals involving shear strain, where the symmetry is lowered from C_6 to C_2, and the transformation strain appears in the basic plane. Let the principal axis C_6 be oriented in the z direction. These kinds of hexagonal to orthorhombic transformations have been discussed, for example, by Wen *et al* [30–33]. They developed a phase field model in the spirit of Khachaturyan [34] and found experimental evidence for the patterns predicted by their phase field simulation results for microstructures in Ti–Al–Nb systems.

Although the general approach presented above is valid also in more general three-dimensional cases, we assume from now on that the system obeys translational invariance in the z direction, and thus it is effectively two-dimensional. By a

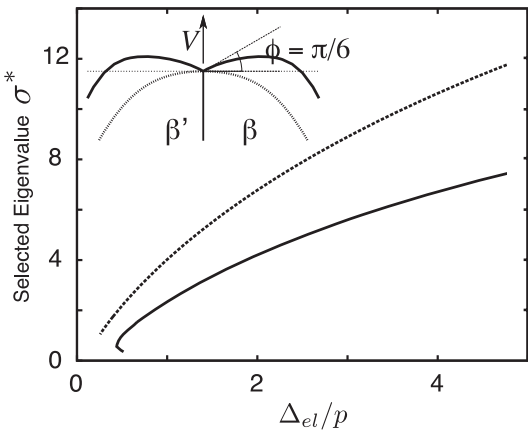

Figure 6. Stability parameter σ^* versus $\Delta_{\rm el}/p$ for two values of ϕ: the dashed line corresponds to $\phi = 0$ and the solid line corresponds to $\phi = \pi/6$. The inset shows numerical results for the tip shapes of the corresponding two different bicrystals.

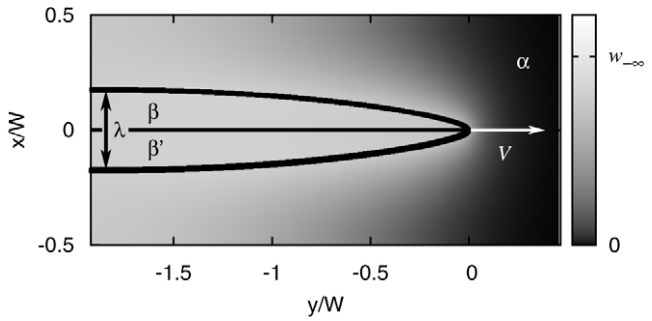

Figure 7. Geometrical set-up of a bicrystal growing with a velocity V in a finite channel of width W. The interface contours are indicated by the solid lines. Initially, the metastable phase α is undercooled and has the dimensionless temperature $w = 0$. Asymptotically far behind the tip, where the interface does not move any more due to the thermal insulation, the asymptotic fraction λ of the new phase and the constant temperature $w_{-\infty}$ of the tail region can be measured. The α/β and α/β' interface contour and the temperature field (illustrated by the grayscaling) are obtained by phase field simulations. For the considered case $\gamma_{\rm b} \ll \gamma$ we have $\phi = 0$ here.

proper choice of the crystal orientation around the main axis in the initial phase, we obtain the new phase in three possible states. In particular, we consider here only the case of the following non-vanishing components of the strain tensor ϵ^0_{ik}:

$$\epsilon^0_{xx} = -\epsilon^0_{yy} = \varepsilon/2, \qquad \epsilon^0_{xy} = \mp\varepsilon\sqrt{3}/2, \tag{12}$$

which can appear here in two 'twinned' orientations. Because the elasticity of hexagonal crystals is axisymmetric in the harmonic approximation and $\epsilon^0_{iz} = \epsilon_{iz} = 0$, we can use the isotropic theory of elasticity, i.e. the expressions ((6) and (7)) for the free energy. The moduli of the effective isotropic elasticity can then be expressed in terms of the elastic constants of the original hexagonal crystal. Eliminating the thermal field, we obtain the steady-state equation for the shape of the solid–solid interface [9]. In the co-moving frame of reference, this equation is

$$\Delta - \frac{d_0\kappa}{R} + \frac{T_{\rm eq}C\delta\tilde{F}^{\rm el}}{L^2} = \frac{p}{\pi}\int {\rm d}x'\, \exp[-p(y(x) - y(x'))]K_0(p\eta), \tag{13}$$

where $\eta = [(x - x')^2 + (y(x) - y(x'))^2]^{\frac{1}{2}}$, K_0 is the modified Bessel function of third kind in zeroth order and $p = VR/2D_{\rm t}$ is the Peclet number, with R being the tip radius of the asymptotic Ivantsov parabola.

The mismatch between the phases induces an elastic hysteresis, which motivates the definition of a shifted undercooling:

$$\tilde{\Delta} = \Delta - \Delta_{\rm el}, \qquad \Delta_{\rm el} = T_{\rm eq}CE\varepsilon^2/8(1-\nu^2)L^2. \tag{14}$$

The dimensionless parameter $\Delta_{\rm el}$ describes the strength of the elastic effects. The relation between this shifted undercooling $\tilde{\Delta}$ and the Peclet number is given by the two-dimensional Ivantsov formula [1], $\tilde{\Delta} = \sqrt{p\pi}\exp(p){\rm erfc}(\sqrt{p})$.

Notice that, without elastic effects, this problem is equivalent to the classical dendritic growth problem with isotropic surface tension. The latter does not have a solution with kink-free dendrite tips [3, 35]. For example, Meiron [35] calculated the tip kink angle ϕ as a function of the 'stability parameter' $\sigma = d_0/pR$ for several values of the Peclet number with isotropic surface tension numerically and found that ϕ is negative for any positive value of σ.

Now, we discuss the numerical results obtained by the solution of equation (13) in the spirit of [35]. First, we point out that, for the investigated case of shear transformations, the new phase appears as a bicrystal with the two opposite orientations, as depicted in figure 7. The presence of the twin cancels a macroscopic shear strain far behind the tip, which would otherwise be thermodynamically unfavorable. The twin boundary energy is denoted by $\gamma_{\rm b}$, and together with the α/β grain boundary energy it determines the tip angle ϕ, which is defined in the inset of figure 6. In the important regime of small Peclet numbers, the eigenvalue $\sigma = \sigma^*(\phi, \Delta_{\rm el}, p)$ depends only on the ratio $\Delta_{\rm el}/p$ for a fixed angle ϕ. While the strength of the elastic effects is assumed to be small, $\Delta_{\rm el} \ll 1$, the control parameter $\Delta_{\rm el}/p$ can be varied in a wide range in the limit of small p. The eigenvalue σ^* as a function of $\Delta_{\rm el}/p$ for two values of the angle, $\phi = 0$ and $\pi/6$, is shown in figure 6. The situation with $\phi \approx 0$ is realized if $\gamma_{\rm b} \ll \gamma$, and formally it corresponds also to conventional dendritic growth with a smooth tip, but here with selection due to elasticity. The other case, $\phi \approx \pi/6$, corresponds to $\gamma_{\rm b} \approx \gamma$. The Poisson ratio is here fixed to $\nu = 1/3$.

The most remarkable feature of these results is that we do find dendritic solutions even for *isotropic surface tension* in the presence of the elastic effects. In this sense, the elastic effects serve as a new selection mechanism. We note that σ^* becomes large for large values of $\Delta_{\rm el}/p$, while in the classical dendritic growth σ^* is always small, being controlled by tiny anisotropy effects, see also section 2. Thus, the growth velocity, $V = 2D_{\rm t}\sigma^* p^2/d_0$, can be much larger due to elastic effects, compared to classical dendritic growth.

4.4. Channel growth

The growth in a channel of finite width W differs significantly from the free growth scenario discussed above. Here, the specific behavior depends, of course, on the choice of boundary conditions for the displacements and the temperature field at the channel walls. As shown in figure 7, the bicrystal pattern, consisting of two β phases with opposite orientations of the eigenstrain, is growing with a velocity V into the metastable phase α, which is initially at the undercooling temperature T_∞.

To obtain a thermodynamically stable multiphase state in the tail region, we assume thermal insulation along the channel walls, i.e. $\partial w/\partial x = 0$. Notice, that in contrast to the isothermal situation discussed in [36], the temperature $w_{-\infty}$ in the tail region is not a control parameter and has to be found self-consistently. Here, we investigate the two-dimensional plane strain bicrystal growth in a stress-free channel, i.e. the following elastic boundary conditions are obeyed:

$$\sigma_{xx}(x = \pm W/2) = 0, \qquad \sigma_{xy}(x = \pm W/2) = 0. \tag{15}$$

Recently, we also studied channel growth in a confined strip with fixed boundary conditions for the displacements [37]. Mechanical equilibrium and coherence at the interface lead to a discontinuous jump in the normal and shear components of the strain tensor [9]. This causes non-vanishing homogeneous strains in the β and β' phases in the tail region:

$$\epsilon_{xy}^{(\beta)} = \epsilon_{xy}^{0}, \qquad \epsilon_{xx}^{(\beta)} = \epsilon_{xx}^{0} + \frac{\nu}{1-\nu}(\epsilon_{yy}^{0} + \epsilon_{zz}^{0}) \tag{16}$$

and results in the non-zero stress component:

$$\sigma_{yy}^{(\beta)} = \frac{-E}{1-\nu^2}(\epsilon_{yy}^{0} + \nu\epsilon_{zz}^{0}). \tag{17}$$

Notice that there is also a similar non-vanishing stress component σ_{zz} due to the plain strain geometry. Next, we calculate the energy excess $\delta\mathcal{F}$, due to the appearance of a finite fraction of the new phase λ. It is defined as the difference between the energy for $\lambda = 0$ without any β-phase pair (i.e. far ahead of the tip) and the energy with an arbitrary but finite fraction (in the tail region):

$$\delta\mathcal{F} = -W(\tfrac{1}{2}\lambda F_{\mathrm{el}}^{(\beta)} + \tfrac{1}{2}\lambda F_{\mathrm{el}}^{(\beta')} + (1-\lambda)F_{\mathrm{el}}^{(\alpha)}) - 2\gamma - \gamma_{\mathrm{b}} + W\int_0^{\lambda}\left(\frac{L(T_{\mathrm{eq}} - T(\lambda'))}{T_{\mathrm{eq}}}\right)\mathrm{d}\lambda'. \tag{18}$$

Initially, there is only the elastically relaxed but metastable phase α at the constant temperature $w = 0$. As soon as we have a finite phase fraction λ, the energy increases by elastic and capillary contributions. Since we again assume the grain boundary energy γ_{b} to be much smaller than the boundary energy γ between α and β or β', its contribution to the energy excess can be neglected. Finally, the integral appears due to thermal insulation, since an increase of the amount of β phases leads to the release of latent heat, and therefore causes an increase of the temperature. Using the heat conservation condition we find the relation between the asymptotic temperature and the phase fraction to be

$$T(\lambda) = T_\infty + \lambda\frac{L}{C}. \tag{19}$$

Therefore, we obtain for the energy excess as a function of the asymptotic phase fraction λ

$$\delta\mathcal{F}(\lambda) = \frac{WL^2}{CT_{\mathrm{eq}}}\left((\Delta - \Delta_{\mathrm{el}})\lambda - \frac{1}{2}\lambda^2 - \frac{2d_0}{W}\right), \tag{20}$$

where the parameter Δ_{el}, as already introduced above in equation (14), defines the strength of elastic effects. The maximum of this energy excess, $\partial\Delta F(\lambda)/\partial\lambda = 0$, determines the asymptotic equilibrium fraction in the tail region, which expresses the thermodynamic balance between elastic deformation and free energy release due to the phase transition:

$$\lambda = \Delta - \Delta_{\mathrm{el}}. \tag{21}$$

If the fraction λ is in the range $0 < \lambda < 1$, we obtain phase coexistence in the asymptotic regime far behind the tip. Since the equilibrium fraction λ and the asymptotic tail temperature $w_{-\infty}$ coincide (see equation19), this equation describes again the elastic hysteresis, which is also reflected by its similarity with equation (14).

Additionally, the growth of the β phases demands that the energy excess (20) for the equilibrium fraction (21) has to be positive:

$$\delta\mathcal{F}(\lambda) = \frac{WL^2}{CT_{\mathrm{eq}}}\left(\frac{1}{2}\lambda^2 - \frac{2d_0}{W}\right) > 0. \tag{22}$$

This is equivalent to the condition $\lambda > \lambda_{\mathrm{crit}}$, where λ_{crit} is given by

$$\lambda_{\mathrm{crit}}^2 = \frac{4d_0}{W}. \tag{23}$$

4.5. Phase field modeling

To solve the full free boundary problem numerically in the channel geometry, we use a phase field formulation. For a review of this method see, for example, [21] and references therein. Phase field modeling techniques have proved their value not only for solidification, but are also successfully applied to solid-state transformations (see, e.g., [38]). Recently, more complex phase field models for solid–solid transformations have been developed, allowing us to study, for example, three-dimensional situations with more than two phases, full anisotropy of elasticity and surface tension, or simulations beyond the symmetrical model, where the two phases have different diffusion and elastic constants [39, 40].

For the purpose of the present paper, we consider the bicrystal configuration within a symmetrical model of diffusion-limited solid–solid phase transitions with isotropic surface tension, which was introduced above. Immediately taking into account the symmetry along the grain boundary plane and describing only either the upper or lower half of the strip, we also avoid the formulation of more complicated multiphase descriptions.

Formulating an appropriate two-phase model, we first introduce the phase field φ, which will discriminate between the different phases. We define $\varphi = 1$ for the metastable initial

phase α and $\varphi = 0$ for the new phase β or β', respectively. We start from a free energy functional, similar to [41]

$$F[\varphi, w, u_i] = \int_V (f_s + f_{dw} + f)\, dV, \tag{24}$$

where $f_s(\nabla\varphi) = 3\gamma\xi(\nabla\varphi)^2/2$ is the gradient energy density and $f_{dw}(\varphi) = 6\gamma\varphi^2(1-\varphi)^2/\xi$ is the double-well potential, guaranteeing that the free energy functional has two local minima at $\varphi = 0$ and 1 corresponding to the two distinct phases of the system. The form of the double-well potential and the gradient energy density are chosen such that the phase field parameter ξ defines the interface width and the parameter γ corresponds to the interface energy of the sharp interface description [42]. The free energy density $f(\varphi, w, u_i)$ of our phase field description has a φ-dependent eigenstrain tensor, such that we obtain the desired bulk free energies equation (6) and equation (7) for $\varphi = 0$ and $\varphi = 1$, respectively:

$$f(\varphi, u_i, w) = \frac{E}{2(1+\nu)}\left(\frac{\nu}{1-2\nu}(\epsilon_{ii} - h(\varphi)\epsilon^0_{ii})^2 + (\epsilon_{ik} - h(\varphi)\epsilon^0_{ik})^2\right) + L\frac{T - T_{eq}}{T_{eq}}h(\varphi), \tag{25}$$

where we choose the interpolation function h to be $h(\varphi) = 1 - \varphi^2(3 - 2\varphi)$. It is the simplest polynomial satisfying the necessary interpolation conditions $h(0) = 1$ and $h(1) = 0$ and having a vanishing slope at $\varphi = 0$ and 1, in order not to shift the bulk states.

The evolution equation of the phase field is given by the variational expression

$$\frac{\partial\varphi}{\partial t} = -\frac{M}{3\gamma\xi}\left(\frac{\delta F}{\delta\varphi}\right)_{u_i, w}. \tag{26}$$

For large values of the mobility M we recover the desired case of diffusion-limited growth in the sharp interface limit. The elastodynamic equations are

$$\rho\ddot{u}_i = -\left(\frac{\delta F}{\delta u_i}\right)_{\varphi, w} = \frac{\partial\sigma_{ik}}{\partial x_k}, \tag{27}$$

which recover static elasticity for slowly propagating interfaces in comparison to the sound speed $v_s \sim (E/\rho)^{1/2}$, with ρ being the mass density.

For the temperature field we have the usual thermal diffusion equation with the motion of the phase field or interface being a source of latent heat:

$$\frac{\partial w}{\partial t} = D_t\nabla^2 w + h'(\varphi)\frac{\partial\varphi}{\partial t}, \tag{28}$$

where the prime denotes the derivative with respect to φ. This phase field description is very similar to the model in [43].

Implementing the stress-free boundary conditions equation (15) means that the displacements have to obey the following set of coupled partial differential equations:

$$(1-\nu)\frac{\partial u_x}{\partial x} = -\nu\frac{\partial u_y}{\partial y}, \qquad \frac{\partial u_y}{\partial x} = -\frac{\partial u_x}{\partial y}, \tag{29}$$

which can be achieved, for example, by a simple relaxation method. At the symmetry plane the boundary conditions are $u_x = 0$, $\sigma_{xy} = 0$ and, for the specific case $\gamma_b \ll \gamma$ considered here, $\partial\varphi/\partial x = 0$ [36].

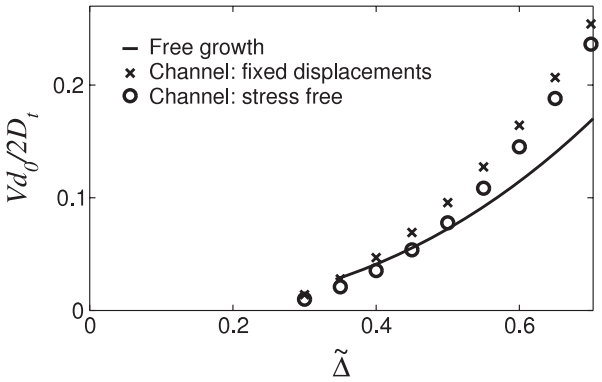

Figure 8. Comparison of growth velocities obtained from Green's function method for the free space geometry for $\phi = 0$ (see figure 6) with the velocities obtained from phase field simulations for the channel geometry. For this simulation the parameters were set as follows: $\Delta_{el} = 0.3$, $W/d_0 = 100$ and $W/\xi = 80$.

Performing a series of phase field simulations of the bicrystal growth in the infinitely compliable channel, we found the same morphology as in the free space geometry, as obtained from the boundary integral method described above. A typical shape of the bicrystal pattern and the corresponding temperature distribution, obtained from phase field simulations, is shown in figure 7. The growth velocity as a function of the driving force $\tilde{\Delta}$ for the free growth (Green's function approach) and for the channel geometry (phase field method), both for a stress-free strip and fixed displacement boundary conditions is shown in figure 8. Here, we mention that the asymptotic width of the new phase far behind the tip is different for the more constrained fixed displacement boundary conditions scenario, and growth always starts at a driving force $\tilde{\Delta}$ that is lower for stress-free boundaries, because then the tails can adjust freely and less elastic energy is stored there [37].

In an intermediate regime of driving forces around $\tilde{\Delta} = 0.4$, we obtain good quantitative agreement for the growth velocities of these three different cases shown in figure 8. We mention that the phase field simulations are rather qualitative in the present state, as the results are still affected by the finite interface and channel width. In particular, for convergence towards the sharp interface results of Green's function method, the fraction of β phases should be infinitely small. For more detailed investigations the generalization of the phase field model to thin interface asymptotics in the spirit of [44] is desirable.

5. Summary and conclusion

In this paper we discussed the propagation of dendritic growth fronts in a context different from solidification. Namely, for the inverse problem, melting of an alloy, diffusive transport within the solid phases is slow, and therefore alternative transport mechanisms can play the dominant role. We discussed different melting scenarios in homogeneous and heterogeneous systems with the common feature that, far behind the tip, the

shape of the melting front becomes parabolic. The presence of elastic effects can affect the driving force in the case of partial melting with two advancing fronts—a melting and a solidifying interface—which is then not only controlled by the undercooling. There, in particular, strong concentration gradients ahead of the melting front provoke coherence stresses that shift the thermodynamic equilibrium and therefore provide an impurity flux in the melt; consequently, the front propagation is here much faster than for diffusion in the solid phase. Another important finding is that grain boundaries can change the selection mechanisms, since steady-state growth is possible even without the anisotropy of surface tension, in contrast to conventional dendritic growth. This behavior, together with a rotation of the triple junction, is also qualitatively observed in phase field simulations of peritectic and eutectic alloys.

Elastic effects naturally become more important during solid-state transformation, mainly due to density differences and structural changes, and also here we find dendritic patterns without surface energy anisotropy. The growth velocity, which is selected here through the elastic effects, turns out to be significantly higher than for conventional dendritic growth. We investigated in particular the growth of a bicrystal during free growth using Green's function methods and a phase field model for the growth in a channel.

In conclusion, we have demonstrated that, in the context of diffusion-limited dendrite-like transformations other selection mechanisms than surface tension anisotropy, in particular heterogeneities and elastic effects, can become effective and lead to new growth behaviors.

Acknowledgment

This work has been supported by the DFG priority program SPP 1296.

References

[1] Ivantsov G P 1947 *Dokl. Akad. Nauk USSR* **58** 567
[2] Kessler D *et al* 1988 *Adv. Phys.* **37** 255
[3] Brener E A and Mel'nikov V I 1991 *Adv. Phys.* **40** 53
[4] Ben Amar M and Brener E A 1995 *Phys. Rev. Lett.* **75** 561
[5] Ihle T and Müller-Krumbhaar H 1993 *Phys. Rev. Lett.* **70** 3083
[6] Gorbunov A V 1993 *Europhys. Lett.* **24** 773
[7] Asta M *et al* 2009 *Acta Mater.* **57** 941
[8] Brener E A *et al* 2007 *Phys. Rev. Lett.* **99** 105701
[9] Pilipenko D *et al* 2008 *Phys. Rev.* E **78** 060603(R)
[10] Barbieri A and Langer J S 1989 *Phys. Rev.* A **39** 314
[11] Yoon D N and Hupmann W J 1979 *Acta Metall.* **27** 973
[12] Muschik T *et al* 1989 *Acta Metall.* **37** 603
[13] Yoon D N 1995 *Int. Mater. Rev.* **40** 149
[14] Brener E A and Temkin D E 2005 *Phys. Rev. Lett.* **94** 184501
[15] Yoon D N *et al* 1985 *Interface Migration and Control of Microstructures* (Metals Park, OH: American Society of Metals) p 19
[16] Temkin D E 2005 *Acta Mater.* **53** 2733
[17] Saito Y 1996 *Statistical Physics of Crystal Growth* (Singapore: World Scientific)
[18] Brener E A and Temkin D E 2008 *Acta Mater.* **56** 2290
[19] Temkin D E 2005 *Abstracts of ICASP (KTH, Stockholm, June 2005)*
[20] Brener E A and Temkin D E 2007 *Acta Mater.* **55** 2785
[21] Boettinger W *et al* 2002 *Annu. Rev. Mater. Res.* **32** 163
[22] Lo T S *et al* 2003 *Acta Mater.* **51** 599
[23] Parisi A and Plapp M 2008 *Acta Mater.* **56** 1348
[24] Steinbach I *et al* 1996 *Physica* D **94** 135
[25] Nestler B and Wheeler A A 200 *Physica* D **138** 114
[26] Folch R and Plapp M 2005 *Phys. Rev.* E **72** 011602
[27] Gollub J P and Langer J S 1999 *Rev. Mod. Phys.* **71** 396
[28] Privorotskii I A 1971 *Sov. Phys.—JETP* **33** 825
[29] Langer J S 1980 *Rev. Mod. Phys.* **52** 1
[30] Wen Y H *et al* 1999 *Acta Mater.* **47** 4375
[31] Wen Y H *et al* 1999 *Acta Mater.* **48** 4125
[32] Wen Y H 2000 *Phil. Mag.* A **80** 1967
[33] Wen Y H *et al* 2001 *Acta Mater.* **49** 13
[34] Wang Y and Khachaturyan A G 1997 *Acta Mater.* **45** 759
[35] Meiron D I 1986 *Phys. Rev.* A **33** 2704
[36] Brener E A *et al* 2007 *Phys. Rev.* E **75** 041604
[37] Fleck M *et al* 2009 arXiv:0811.2723 [cond-mat]
[38] Chen L Q 2002 *Annu. Rev. Mater. Res.* **32** 113–40
[39] Steinbach I and Apel M 2006 *Physica* D **217** 153
[40] Greenwood M *et al* 2009 *Acta Mater.* **57** 2613
[41] Kassner K *et al* 2001 *Phys. Rev.* E **63** 036117
[42] Gugenberger C *et al* 2008 *Phys. Rev.* E **78** 016703
[43] Slutsker J *et al* 2006 *Phys. Rev.* B **74** 914103
[44] Karma A and Rappel W-J 1996 *Phys. Rev.* E **53** R3017
Karma A and Rappel W-J 1998 *Phys. Rev.* E **57** 4323